CHINA FOUNDRY Research & Development
Vol. 22 No. 4 July 2025
www.springer.com/41230
https://doi.org/10.1007/s41230-025-5034-9

Influence of nodular graphite on microstructure, mechanical properties, and wear behavior of austempered ductile iron

***Xue-bo Zhao, Shu-ya Diao, Yan-song Nan, Jin-hai Liu, and Jing-kun Li**
School of Material Science and Engineering, Hebei University of Technology, Tianjin 300401, China

Abstract: This study systematically investigated the effects of graphite nodule parameters, including count, average diameter, and nodularity, on microstructure and mechanical properties of austempered ductile irons (ADIs). The ADI specimens with graphite nodule counts of 212±11 mm^{-2}, 308±9 mm^{-2}, 415±10 mm^{-2}, and 589±13 mm^{-2} were designated as G-200, G-300, G-400, and G-600, respectively. Results indicate a progressive refinement of graphite with an increase in nodule counts. Specifically, the average nodule diameter decreases from 33.3±1.3 μm for G-200 to 17.0±0.7 μm for G-600. The nodularity of all samples is above 90%. Furthermore, the nodularity exhibits a corresponding increasing trend with the rise of graphite nodule count in ADIs. Additionally, the volume fraction of the austenite phase in ADIs decreases with an increase in graphite nodule count. The graphite nodule count changes the tensile strength and elongation of ADIs. The specimen G-400 exhibits the ultimate tensile strength of 897±11 MPa and an elongation of 9.8%±0.6%, representing 5.3% and 44.1% improvements respectively compared to G-200. To explore the wear resistance of ADIs with different graphite nodule counts, dry sliding friction and wear test of different samples was carried out at room temperature. At a high load of 25 N, G-400 exhibits superior wear resistance, achieving a 42% reduction in worn volume compared to G-200. Worn micromorphology identifies three primary wear mechanisms: microcutting-dominated abrasive wear, adhesive wear, and fatigue wear.

Keywords: austempered ductile iron (ADI); nodular graphite; mechanical property; friction and wear

CLC numbers: TG143.9 **Document code:** A **Article ID:** 1672-6421(2025)04-374-11

1 Introduction

Material wear often leads to wear-related failures, which in turn reduce production efficiency, accelerate equipment deterioration, and compromise product quality. In extreme scenarios, such failures may escalate into equipment malfunctions, production line halts, and even catastrophic safety accidents. Notably, industrially advanced nations experience approximately 30% energy loss attributable to material wear, while China experiences an energy loss of 28% due to component wear, corresponding to an annual economic loss approximating CNY 40 billion[1].

Due to its excellent mechanical and friction performance, the low-cost austempered ductile irons (ADIs) have been an indispensable engineering material in mining, automobile, machinery industries, as well as the renewable energy and new technology industries[2-4]. The outstanding performance of ADIs can be owed to their ausferrite structure and the nodular graphite. Under the harsh conditions characterized by frequent and severe wear, conventional ADIs demonstrate insufficient wear resistance for practical applications. Current research priorities focus on enhancing both the mechanical properties and wear resistance of ADIs to accommodate such wear-intensive environments. Notably, the ADIs with an optimized graphite nodule parameter exhibit enhanced friction-reducing capabilities.

Spheroidal graphite nucleates independently during solidification, with nodular graphite growth occurring in two stages: liquid-phase direct growth (before austenite shell formation) and solid-state diffusion growth (carbon diffusion through the austenite shell to the graphite surface)[5-7]. The formation of nodular graphite has significant influence on both the microstructure

***Xue-bo Zhao**
Lecturer. Her research interests primarily focus on wear resistant cast iron materials.
E-mail: zhaoxueboliu@126.com
Received: 2025-02-12; Revised: 2025-03-06; Accepted: 2025-04-08

and performance of ADIs. It can prevent the precipitation of hazardous carbides that degrade the mechanical properties of ADIs[8]. While, it also influences the ferrite-to-austenite proportion, thereby affecting the mechanical properties[9]. Both the count and morphology of nodular graphite can affect the mechanical and friction properties of the ADIs[10]. Graphite with a higher degree of spheroidization mitigates the stress concentration and crack initiation in the matrix. Adding alloying elements is one of the main methods to control the count and morphology of the nodular graphite in ADIs[11-13]. However, the addition of alloying elements increases the manufacturing cost of ADIs. Moreover, controlling the addition amount of these alloying elements is difficult, which poses disadvantageous for the efficient, continuous production of the ADIs. The previous study found that the characteristics of graphite in ADIs are determined by the solidification process[14]. It has been clarified that the cooling rate is one of the key factors influencing the formation of nodular graphite. A rapid cooling rate during solidification promotes the formation of a great number of smaller graphite nodules[15-17].

By regulating the cooling rates during the solidification process, ADI specimens with varying nodule counts along the height direction were successfully manufactured. It is of paramount importance to investigate how parameters such as graphite nodule count, average diameter, and nodularity impact the microstructure, mechanical properties, and friction behavior of ADI. This research not only contributes to a deeper understanding of the relationship between material microstructure and macroscopic properties but also provides theoretical guidance for industrial production, thereby facilitating the innovation and application of high-performance ADI materials.

2 Experimental procedure

2.1 Casting

Commercial pig iron, steel, ferrosilicon, ferromanganese, and electrolytic copper were employed as the raw materials, and the chemical composition of the ADI is illustrated in Table 1. The raw materials were melted in a medium-frequency induction furnace. After the molten iron is completely melted, the $FeSiMg_8Re_3$ alloy was added as a nodulizer, along with silicon-barium as an inoculant, each at 0.3wt.%. The melt was heated to 1,530 °C and holding for 15 min. Prior to pouring, the temperature was monitored and kept between 1,510 °C and 1,560 °C using an NSP-1212R temperature-measuring gun. To minimize thermal shrinkage defects, enhance heat dissipation, and establish a unidirectional temperature gradient, chills were placed at the bottom of the mold. The cooling rate of the ingot changes along the pouring direction (height direction) by placing chills at the bottom of the mold. Theoretically, the maximum cooling rate occurs near the chilled surface, resulting in the highest graphite nodule count. Progressing upward through the ingot height, the cooling rate gradually diminishes, accompanied by a corresponding reduction in graphite nodule count. The final product was a block with dimensions of 100 mm×70 mm×35 mm (height), as shown in Fig. 1.

Table 1: Chemical composition of the ADI sample

Element	C	Si	Mn	P	S	Cu	Mg
Content (wt.%)	3.6	2.41	0.23	0.036	0.011	0.65	0.045

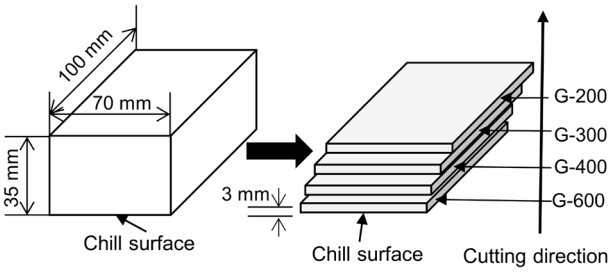

Fig. 1: Schematic diagram of ADI samples

2.2 Austempering

The cast ADI block was heated to 890 °C and helding for 90 min in a box resistance furnace. Then, it was quenched to 280 °C and helding for 60 min in a salt bath consisting of 50% $NaNO_3$ and 50% $NaNO_2$. The ADI samples were extracted from the salt bath and subsequently air-cooled to room temperature. Then, as shown in Fig. 1, the ADI samples with dimensions of 100 mm×70 mm×3 mm were cut from the chill surface towards the interior to characterize the microstructure and mechanical properties of ADI samples with different graphite nodule parameters. Table 2 lists the graphite nodule count of ADI at different heights from the chill surface. The research findings indicate that the nodule count decreases as the distance from the chill surface increases. The ADI specimens with average graphite nodule counts of 212±11 mm^{-2}, 308±9 mm^{-2}, 415±10 mm^{-2}, and 589±13 mm^{-2} were designated as G-200, G-300, G-400, and G-600, respectively.

Table 2: Graphite nodule count of ADIs at different heights from the chill surface

Samples	Distance from the chill surface (mm)	Average nodule count
G-600	0–3	589±13
G-400	3–6	415±10
G-300	6–9	308±9
G-200	9–12	212±11

2.3 Microstructure characterization

The count and nodularity of the nodular graphite in ADIs were statistically analyzed using the metallurgical analysis software (LAMOS Master) of an optical microscope (OM, DM2700, Leica, Germany). The microstructure, fracture morphology, and the wear track of the samples were examined using scanning electron microscopy (SEM, SU3800, Hitachi, Japan). The SEM samples underwent etching using a 4% nitric acid alcohol solution following polishing, in order to assess their microstructure.

The graphite nodule count per square millimeter (n_F) was calculated by observing the entire inspected surface and selecting eight representative fields of view. The final average value was then taken. The calculation equation is expressed as Eq. (1)[18]:

$$n_F = \frac{n}{A} \times F^2 \quad (1)$$

where A represents the measured grid area (unit: mm²), F means the magnification factor of the field of view, n is the number of graphite nodules within a single field of view.

The nodularity is defined as the percentage of the sum of all graphite nodules multiplied by their corresponding spheroidal graphite correction factors relative to the total graphite nodule count. The formula is expressed as Eq. (2)[18]:

$$\text{Nodularity} = \frac{1\times n_{1.0} + 0.8\times n_{0.8} + 0.8\times n_{0.6} + 0.8\times n_{0.3} + 0\times n_0}{n_{1.0} + n_{0.8} + n_{0.6} + n_{0.3} + n_0} \times 100\% \quad (2)$$

where $n_{1.0}$, $n_{0.8}$, $n_{0.6}$, $n_{0.3}$, n_0 refer to the counts of graphite nodules assigned to spheroidal graphite correction factors of 1.0, 0.8, 0.6, 0.3, and 0, respectively. The spheroidal graphite correction factor for each graphite nodule was determined by calculating its area ratio (R_a) using the metallographic analysis software of the optical microscope. The area ratio was subsequently converted into a spheroidal correction factor based on the criteria outlined in Table 3. The area ratio (R_a) of an individual graphite particle is calculated as Eq. (3)[18]:

$$R_a = \frac{A_g}{A_c} \quad (3)$$

where A_g means the actual area of the graphite particle, A_c is the area of the smallest circumscribed circle enclosing the particle.

Table 3: Spheroidal correction coefficients corresponding to graphite area ratio[19]

Graphite area fraction (%)	>0.81	0.80–0.61	0.60–0.41	0.40–0.21	<0.20
Spheroidal graphite correction factor	1.0	0.8	0.6	0.3	0

X-ray diffraction (XRD, Smartlab, Rigaku, Japan) was carried out at a scan speed of 6°·min^{-1} ranging from 10° to 90°. The volume fraction of austenite and ferrite in ADI was determined by direct contrast method using the integral intensities of (110), (211), and (200) planes of ferrite and (200), (111), and (220) planes of austenite. The (200) crystallographic plane of the γ-phase (austenite) and the (211) plane of the α-phase (ferrite) were selected for analysis. The peak intensities were recorded to calculate the carbon content in retained austenite and its volume fraction. The volume fractions of retained austenite (V_γ) and ferrite (V_α) were determined using Eqs. (4) and (5)[20]:

$$V_\gamma = \frac{1 - V_c}{1 + K_\gamma \frac{I_\alpha}{I_\gamma}} \quad (4)$$

$$V_\alpha = \frac{1 - V_c}{1 + K_\alpha \frac{I_\gamma}{I_\alpha}} \quad (5)$$

where V_γ, V_α, and V_c refer to the volume fractions of austenite, ferrite, and carbide, respectively; K_γ and K_α denote the reference intensities for the γ-phase and α-phase; I_γ and I_α are the integrated intensities of the γ-phase and α-phase diffraction peaks. Given that the carbide content is negligible, it was assumed that V_c=0 in the calculations.

The lattice parameters of austenite are obtained from the following Eq. (6):

$$\alpha_\gamma = \frac{\lambda\sqrt{H^2 + K^2 + L^2}}{2\sin\theta} \quad (6)$$

where α_γ means the lattice parameter of austenite, H, K, and L represent the diffraction planes corresponding to the diffraction peaks, θ is the diffraction angle, and λ refers to the wave length. The carbon content (C_γ) of the austenite could be calculated by Eq. (7)[21]:

$$\alpha_\gamma = 0.3548 + 0.0044 C_\gamma \quad (7)$$

2.4 Mechanical and wear properties test

The microhardness was tested using a micro-hardness tester (MHT, HMV-G-XY-S, Shimadzu, Japan) with a load of 98.07 mN and holding for 15 s. For each sample, 10 points were selected on the grain boundaries to eliminate errors. The average value of microhardness was recorded.

As shown in Fig. 2, the tensile samples were machined to a dog-bone shape with cross-sectional dimensions of 10 mm×3 mm and a gauge length of 20 mm. The tensile tests were carried out at ambient temperature by using a universal testing machine (UTM, E45.105, MTS, America). Three tensile tests were conducted on each ADI sample, and the average values were recorded.

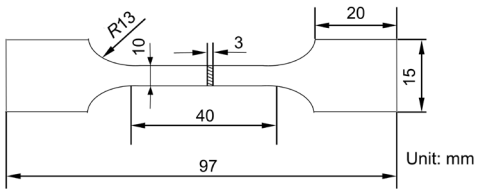

Fig. 2: Schematic diagram of the tensile sample

The wear resistance was measured by linear reciprocating friction and wear (LRFW, CFT-1, Zhongke-Kehua, China). GCr15 steel ball was selected as friction pair, and the normal loads were set as 5 N, 15 N, and 25 N, respectively. The sliding distance was 5 mm, the test duration was 20 min, and the sliding rate was 0.02 m·s^{-1}. The wear tracks of ADIs were obtained using a white light interferometer (WLI, GT-X, Bruker, Germany), and the worn volume of the wear tracks was calculated. The friction and wear tests for each ADI sample were conducted in triplicate.

3 Results and discussion

3.1 Microstructure

Figure 3 shows the size and morphology of the nodular graphite in ADI samples with different graphite nodule counts. Figure 4 presents the diameter of nodular graphite, nodularity, and graphite fracion of ADI samples with different graphite nodule counts. The average diameter of nodular graphite is 33.3±1.3 μm for G-200, 28.1±0.2 μm for G-300, 24.1±0.5 μm for G-400, and 17.0±0.7 μm for G-600 samples. The corresponding nodularity is 94.6±0.8%, 96.2±0.6%, 97±0.2%, and 98.2±0.3%, respectively. The graphite fraction in all ADI samples is around 8.2%, with no significant differences observed. Since the cooling rate during solidification is decreased from the chill surface to the free surface, the nodule count is correspondingly decreased. During crystallization, the nucleation of nodular graphite could be promoted while the growth of nodular graphite could be prevented by a rapid cooling rate, resulting in more finer nodular graphite[22, 23].

Figure 5 shows the microstructure of ADIs with different graphite nodule counts. The microstructure of ADIs consists of graphite nodules, acicular ferrite, and blocky austenite, with the austenite typically being distributed between the acicular ferrite regions. Similar to the characteristics associated with graphite, the ferritic grain size undergoes a progressive diminution with increasing solidification rates, a phenomenon that has been empirically validated in the literature (for wall thicknesses ranging from 25 to 75 mm)[24]. The G-200 sample exhibits the largest grain size of ferrite. With the increase in the number of graphite nodules, the ferrite grains are refined. This is because that during the austempering process, ferrite nucleates on the interfaces of graphite/austenite. These interfaces were broadened by numerous fine graphite nodules, resulting in the improvement of nucleation rate and the refinement of ferrite.

The XRD patterns in Fig. 6(a) illustrates the phase constitution of ADI samples. All the samples are composed of graphite, α (ferrite) phase, and γ (austenite) phase. The α phase is characterized by a bcc structure, while the γ phase exhibits a fcc structure based on phase indexing[25]. According to the minimum energy principle, the ferrite phase exhibits a preference for orientation along the (200) plane, whereas the

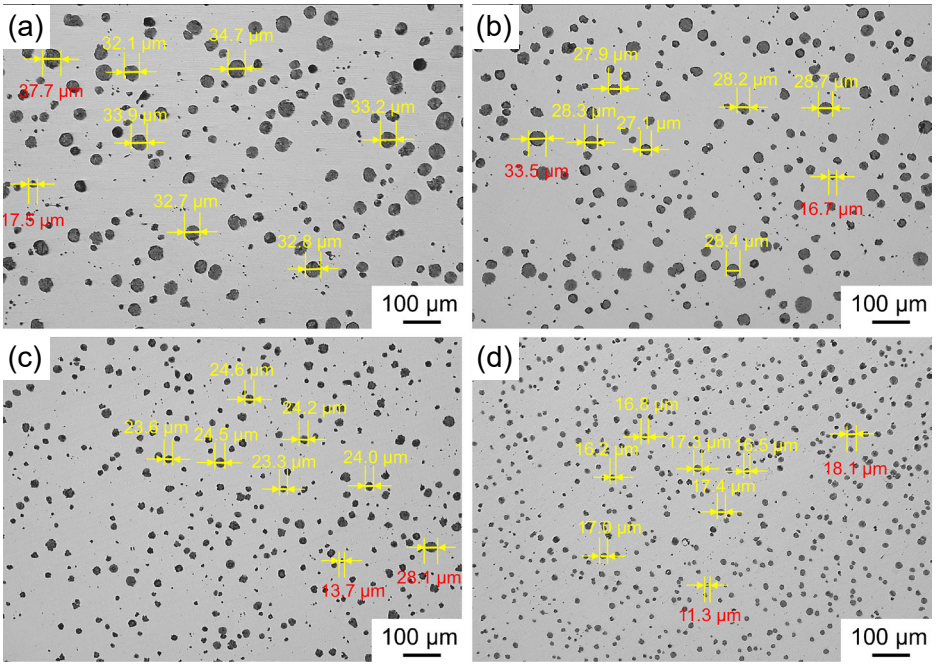

Fig. 3: Morphologies of nodular graphite in different ADI samples: (a) G-200; (b) G-300; (c) G-400; (d) G-600

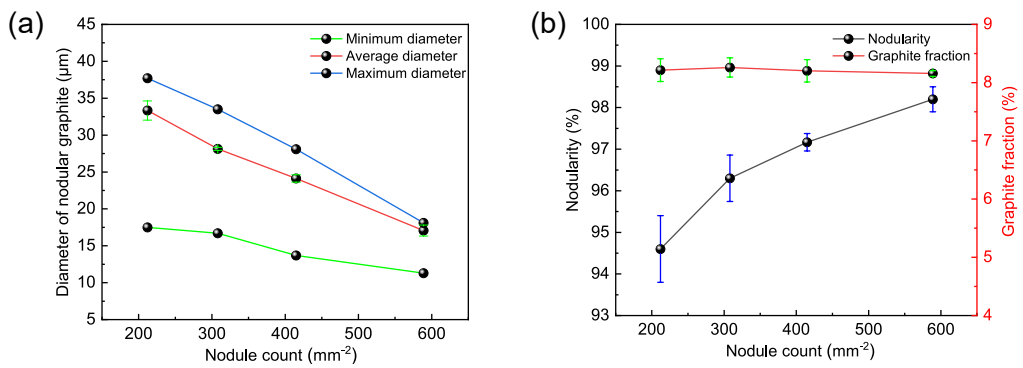

Fig. 4: Diameter of nodular graphite (a) and nodularity and gaphite fraction (b) of ADI samples

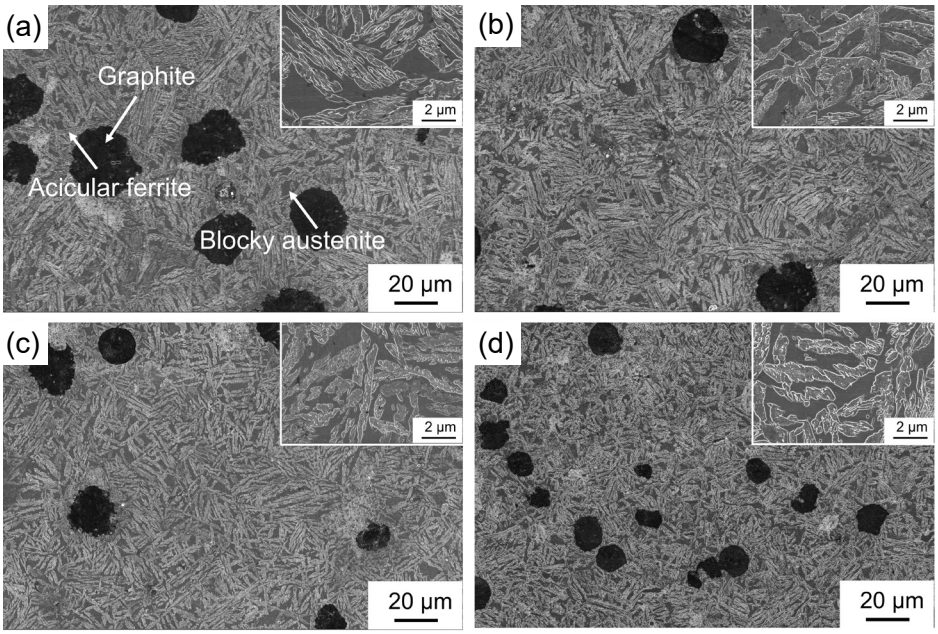

Fig. 5: Microstructures of ADI samples: (a) G-200; (b) G-300; (c) G-400; (d) G-600

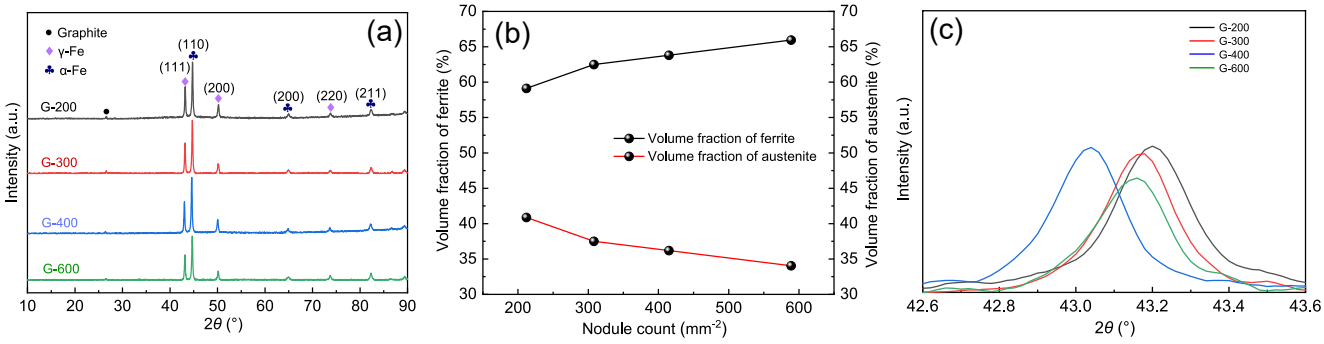

Fig. 6: XRD patterns of ADI samples (a), volume fraction of ferrite and austenite versus nodule count in ADI samples (b), and peak of the (111) crystal plane of austenite (c)

austenite phase demonstrates a tendency towards orientation on the (220) plane. Figure 6(b) illustrates the volume fraction of ferrite and austenite. It demonstrates that the volume fraction of ferrite increases while austenite decreases with the increase of graphite nodules. The increase in the number of graphite nodules provides more nucleation sites, accelerating the nucleation rate of ferrites[26]. This leads to an increase in the volume fraction of ferrite.

Figure 6(c) displays the diffraction peak corresponding to the (111) plane of austenite. As the graphite nodule count increases, the diffraction peak initially shifts toward lower angles and subsequently toward higher angles.

The interplanar spacing of austenite is governed by lattice expansion induced by carbon solid solution[27]. When the number of graphite nodule count is small, the cooling rate is low and carbon atoms have sufficient time to diffuse into the austenite phase. The incorporation of carbon atoms into austenite results in lattice expansion, thereby increasing the interplanar spacing and causing a low-angle shift of the diffraction peak. However, the G-600 sample exhibits the excessive graphite nodule count. The excessive nodules provide additional nucleation sites for ferrite. During the austenite-to-ferrite transformation, carbon atoms are expelled from austenite, leading to a reduction in carbon content within the austenite. This diminishes the lattice expansion effect caused by carbon solid solution. Consequently, the interplanar spacing of austenite decreases, resulting in a high-angle shift of the diffraction peak.

Figure 7 shows the evolution of the carbon content in austenite versus the nodule count. As the concentration of nodular graphite increases, the carbon content of the austenite initially rises and then declines. The carbon content of austenite reaches the ultimate value of 2.088% when the count of nodular graphite is 400 mm^{-2}. As the most common interstitial solution element, carbon plays a crucial role in substantially enhancing the stability of austenite[28]. With the increase of carbon content in austenite, the stability of the austenite is improved, and the formation tendency of ferrite is weakened. Carbon atoms are precipitated from ferrite and enriched in untransformed austenite during ferrite growth[25]. As the graphite nodule count continues to increase, an increased amount of ferrite forms and precipitates carbon atoms. However, the amount of carbon atoms absorbed by austenite is limited, resulting in a decrease in carbon content.

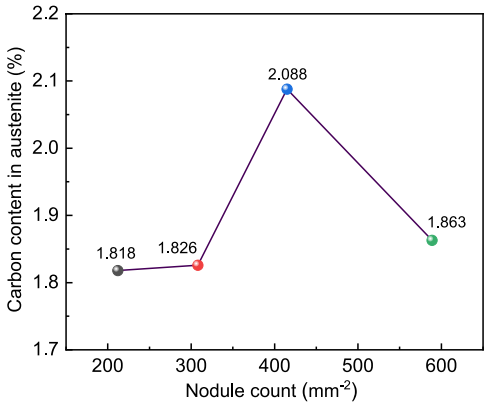

Fig. 7: Evolution of carbon content in austenite versus nodule count

3.2 Mechanical properties

The microhardness of the ADI samples is shown in Fig. 8. The microhardness is 314 $HV_{0.01}$ for G-200, 341 $HV_{0.01}$ for G-300, 392 $HV_{0.01}$ for G-400, and 449 $HV_{0.01}$ for G-600. The results demonstrate that the microhardness increases with an increase in the count of nodular graphite. Since the coarse ferrite grains have less obstruction to dislocation motion[29], the G-200 sample exhibits a lower hardness. The ferrite grains become finer with an increase in nodule count (Fig. 5). Small grain size will form a larger grain boundary area, which can effectively hinder the dislocation motion, thus the G-600 sample demonstrates a relatively higher hardness.

The engineering stress-strain curves of the ADIs are shown Fig. 9, while the related tensile properties are summarized in Table 4. The G-400 sample exhibits the most excellent comprehensive mechanical properties, with the ultimate tensile strength of 897±11 MPa and an elongation of 9.8±0.6%. The elastic modulus of G-400 sample attains its maximum value of 173±7 GPa. A high elastic modulus reduces deformation under a load and effectively enhances dimensional stability.

The differences among the mechanical properties of ADI samples are mainly attributed to the interaction between the matrix microstructure and the nodular graphite. Firstly, fine grains effectively impede crack propagation, improving the plasticity of the material[30]. The G-200 sample exhibits a

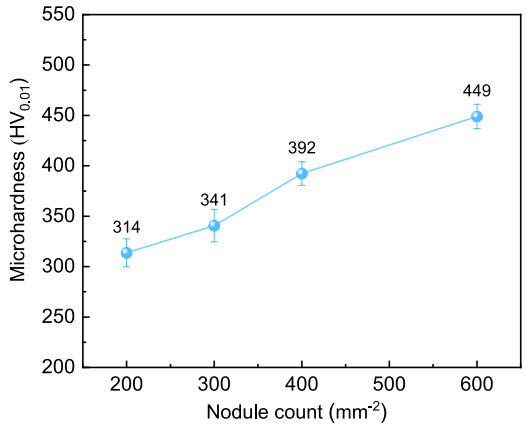

Fig. 8: Microhardness evolution of ADI samples versus nodule count

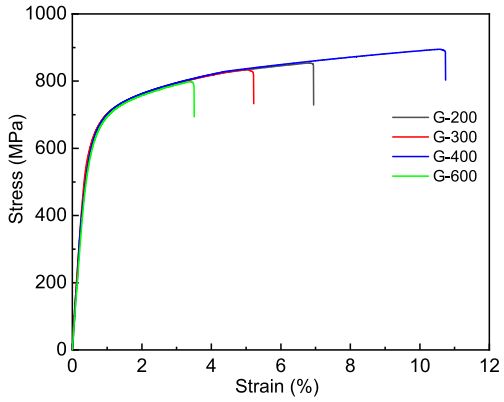

Fig. 9: Engineering stress-strain curves of ADI samples with different nodule counts

Table 4: Mechanical properties of ADI samples with different nodule counts

Samples	Yield strength (MPa)	Ultimate tensile strength (MPa)	Elongation (%)	Elastic modulus (GPa)
G-200	637±7	852±10	6.8±0.5	141±9
G-300	636±7	833±9	5.3±0.3	151±11
G-400	608±5	897±11	9.8±0.6	173±7
G-600	623±6	796±8	3.6±0.4	140±6

coarse-grained structure, resulting in inferior tensile properties. Meanwhile, an excessive number and small size of graphite nodules will exacerbate the stress concentration in ADIs, reducing its tensile strength and elongation. Consequently, the G-600 sample demonstrates comparatively poorer tensile properties. Evidently, the G-400 sample has an optimal nodule count and average diameter of graphite nodules, along with a relatively smaller ferrite grain size, thus achieving excellent tensile properties.

Figure 10 shows the tensile fracture morphology of ADI with different nodule counts. Partial detachment of graphite nodules on the fracture surface results in the formation of characteristic dimples, which are indicative of ductile fracture mechanisms [Figs. 10(a), (c), (e), and (g)]. Microcracks and cleavage planes are also present on the fracture surfaces. Meanwhile, secondary micropores, which are one order of magnitude smaller than the dimples, are observed on the fracture surfaces. These micropores are mainly located near the edges of the dimples formed by the detachment of graphite. Micropores initiated at graphite/matrix interfaces progressively coalesce, leading to the formation of secondary dimples [Figs. 10(b), (d), (f), and (h)]. Theoretically, spherical graphite nodules help to reduce microcracks[31, 32]. For samples with a relatively high graphite nodule count, a more uniform distribution of graphite nodules can be observed [Fig. 10(g)]. However, an excessive graphite nodule count will intensify the degree of stress concentration, which reduces the plasticity of ADI.

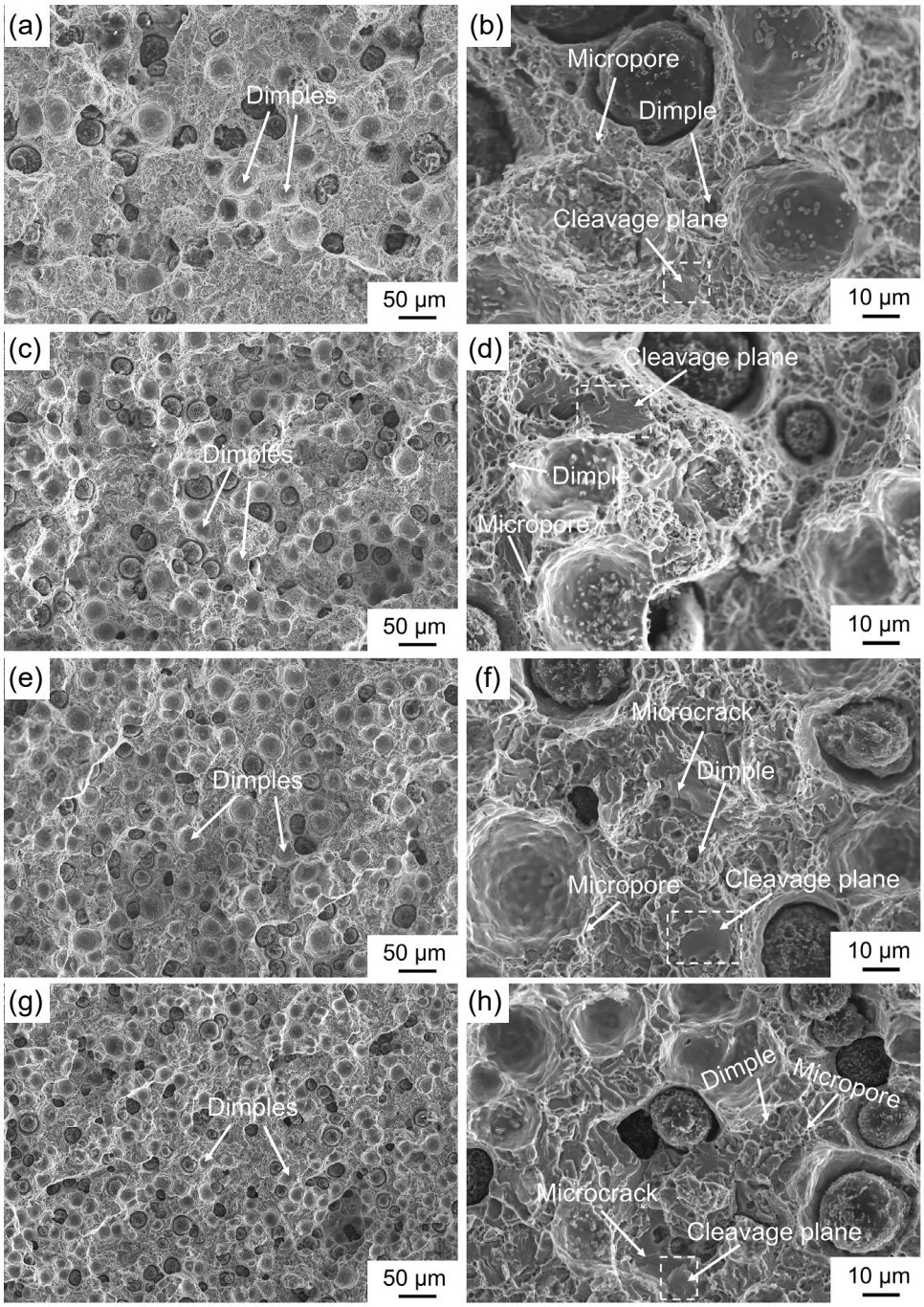

Fig. 10: Tensile fracture morphologies of ADI samples: (a), (b) G-200; (c), (d) G-300; (e), (f) G-400; (g), (h) G-600

3.3 Wear behavior

The friction coefficient curves of ADI samples under different loads are shown in Fig. 11. Under a load of 25 N, the friction coefficient curves of all samples exhibit a relatively high friction coefficient during the running-in stage. During the steady-state wear stage, the friction coefficient remains basically stable. In the severe wear stage (failure stage), the friction coefficient increases suddenly. When the friction pair contacts the sample surface, it is necessary to overcome surface asperities during the movement. Therefore, in the running-in stage, the friction coefficient increases abruptly. As the friction continues, the surface asperities become progressively smoothed. help maintain a relatively stable friction coefficient on the sample surface. In the failure stage (18–20 min), due to the accumulation of debris within the wear tracks, the friction coefficient rises [Figs. 11(a) to (d)].

Figure 12 shows the average friction coefficients of ADI samples under different loads. With the same graphite nodule count, the average friction coefficient of ADI exhibits a decreasing trend with the increase in load. When subjected to loads of 5 N and 25 N, the average friction coefficient gradually decreases as the graphite nodule count increases. Under a load of 15 N, the friction coefficient initially increases and subsequently decreases as the number of graphite nodule increases, reaching its maximum value at G-300. This phenomenon is attributed to the higher accumulation of abrasive within the wear tracks on the surface of the G-300 sample, which consequently elevates the surface friction coefficient.

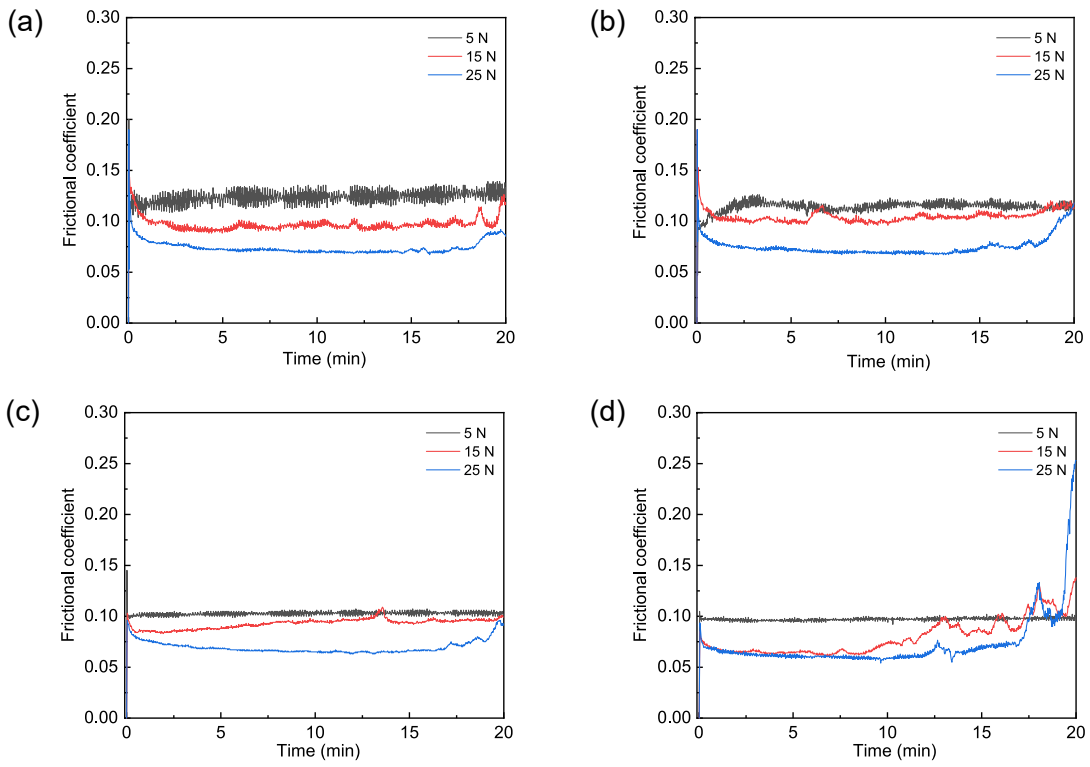

Fig. 11: Friction coefficient curves of ADI samples under different loads: (a) G-200; (b) G-300; (c) G-400; (d) G-600

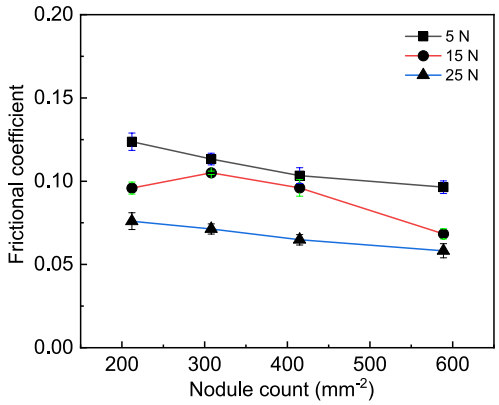

Fig. 12: Average friction coefficients of ADI samples under different loads

Under a load of 25 N, the friction coefficients of G-200, G-300, G-400, and G-600 samples are 0.076, 0.071, 0.064, and 0.058, respectively. During the wear process, more graphite nodules can facilitate the formation of a lubricating film. The enhanced lubricating ability of the lubricating film effectively reduces the average friction coefficient. Meanwhile, the asperities of ADI materials have relatively high microhardness and are not easily flattened during the friction process. As a result, this slows down the rate at which the actual contact area increases. The frictional force is approximately proportional to the normal load and the actual contact area between specimen surface and the friction pair during the loading process[33]. The deceleration in the growth rate of the actual contact area leads to a reduction in the frictional force, thereby reducing the coefficient of friction.

Figure 13 shows the wear morphology of ADI under different loads. The sample surface exhibits relatively minor wear under an applied load of 5 N. The shape of the nodular graphite remains almost unchanged, and shallow grooves and fine debris are observed on the ADI surfaces [Figs. 13(a), (d), (g), and (j)]. This indicates that abrasive wear occurs on the ADI surfaces. Under high load conditions (15 N and 25 N), the morphology of the nodular graphite undergoes significant deformation. Some graphite nodules are completely detached, creating pits on the matrix surfaces. Abrasive particles detach from the surface and cut the surface, resulting in the formation of numerous deep grooves, indicating severe abrasive wear [Figs. 13(k), (l)]. The obvious spalling is observed on the surface of the G-200 sample, as shown in Fig. 13(b). The adhesive wear also occurs on the ADI surface. The graphite nodule count can also influence the wear resistance of ADIs. The presence of an excessive number of graphite nodules in ADIs disrupts the continuity of the matrix microstructure. When subjected to applied stress, microcracks initiate and propagate along the graphite/matrix interfaces [Fig. 13(l)]. This is the phenomenon of fatigue wear, which accelerates wear and thereby diminishes wear resistance.

Figure 14 illustrates the three-dimensional morphology of the ADI samples under 25 N load. The G-200 sample exhibits the deepest plowing grooves, indicating a relatively high degree of abrasive wear on its surface, as shown in Fig. 14(a). Figure 15(a) shows the width and depth of wear track of ADI samples. The wear track depths of the G-200, G-300, G-400, and G-600 samples are measured to be 3.29 μm, 2.71 μm, 2.19 μm, and 2.78 μm, respectively. Similiarly, the wear track widths for these samples are measured to be 229.2 μm, 224.2 μm, 204.6 μm, and 194.2 μm, respectively. Furthermore, the wear scar width progressively decreases with increasing graphite nodule count. Figure 15(b) illustrates the worn volume of ADI samples. As the

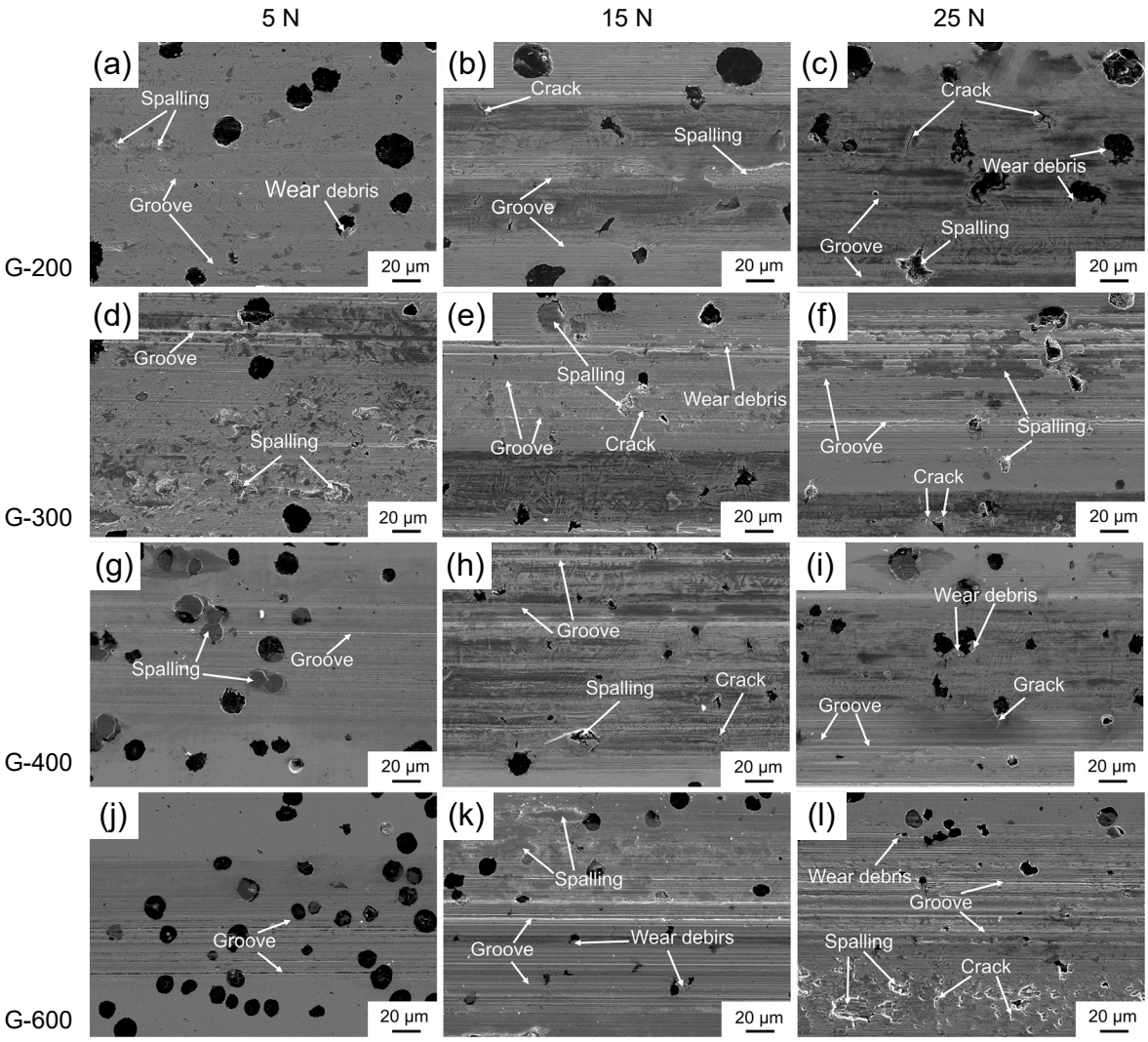

Fig. 13: Wear morphologies of ADI samples under different loads: (a) G-200-5 N; (b) G-200-15 N; (c) G-200-25 N; (d) G-300-5 N; (e) G-300-15 N; (f) G-300-25 N; (g) G-400-5 N; (h) G-400-15 N; (i) G-400-25 N; (j) G-600-5 N; (k) G-600-15 N; (l) G-600-25 N

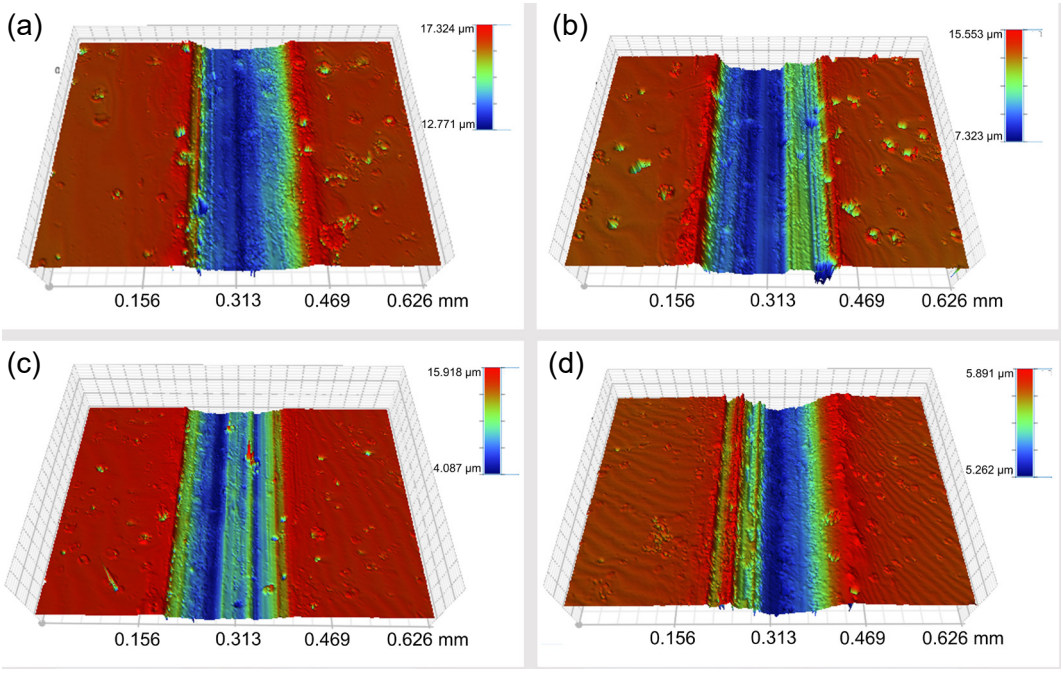

Fig. 14: Three-dimensional morphologies of ADI samples under a load of 25 N: (a) G-200; (b) G-300; (c) G-400; (d) G-600

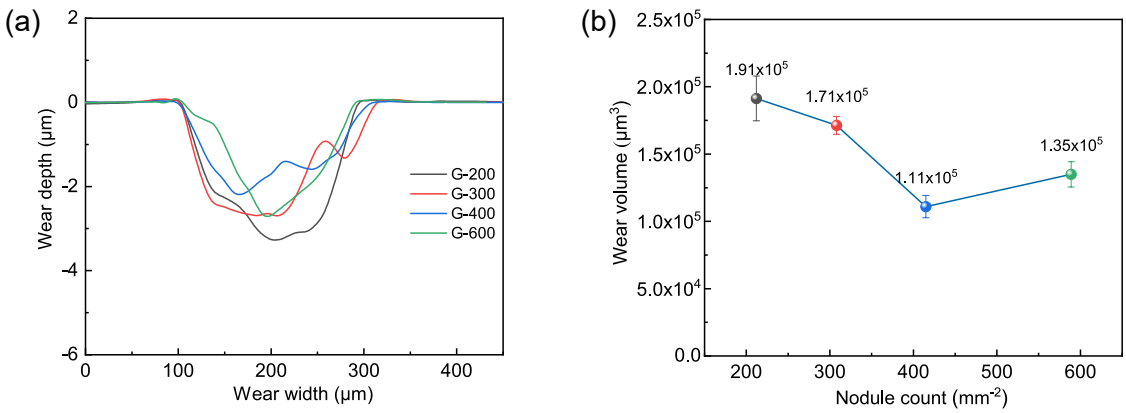

Fig. 15: Width and depth of wear track (a) and worn volume (b) of ADI samples

graphite nodule count gradually increases, the worn volumes are 1.91×10^5 μm³ for the G-200 sample, 1.71×10^5 μm³ for G-300, 1.11×10^5 μm³ for G-400, and 1.35×10^5 μm³ for G-600. The G-400 sample demonstrates the lowest worn volume. This indicates that G-400 sample possesses the most excellent wear resistance properties.

4 Conclusions

(1) When the graphite nodule counts of ADIs increase from 212±11 mm^{-2} to 308±9 mm^{-2}, 415±10 mm^{-2}, and 589±13 mm^{-2}, the average diameter of nodular graphite gradually decreases from 33.3±1.3 μm to 28.1±0.2 μm, 24.1±0.5 μm, and 17.0±0.7 μm respectively. The nodularity of all samples is above 90%. Meanwhile, the increase in graphite nodule count induces progressive refinement of ferritic grains and augmentation in ferrite volume fraction within the ADIs.

(2) The G-400 sample exhibits superior tensile properties owing to its fine-sized ferrite grains and optimal graphite nodule parameters. The graphite nodule parameters of the G-400 sample are characterized by a nodule count of 415±10 mm^{-2}, a nodularity of (97±0.2)%, and an average nodule diameter of 24.1±0.5 μm. Its tensile strength reaches 897±11 MPa, with an enlongation of 9.8±0.6%.

(3) Given that graphite has a lubricating effect, smaller graphite nodules are more easily fragmented and participates in the formation of a lubricating film, thereby reducing the friction coefficient of ADIs. Thus, under the same loads, the friction coefficient decreases with an increase in the graphite nodule count. Under dry friction sliding wear conditions, the G-400 sample exhibits the lowest worn volume. Compared with G-200, which has the largest wear volume, the worn volume of G-400 decreass by 42%. An analysis of the wear morphology reveals that the wear mechanisms of ADIs include abrasive wear, adhesive wear, and fatigue wear.

Acknowledgments

This study was financially supported by the Science and Technology Project of Hebei Education Department (Grant No. BJK2023075), the Science and Technology Project of Tianjin Education Department (Grant No. 2022K1087), and the Chunhui Project Foundation of the Education Department of China (Grant No. HZKY20220264).

Conflict of interest

The authors declare that they have no known competing financial interests or personal relationships that could have appeared to influence the work reported in this paper.

References

[1] Holmberg K, Erdemir A. Influence of tribology on global energy consumption, costs and emissions. Friction, 2017, 5(3): 263–284.
[2] Rimmer A. Application of ADI in a crushed coal delivery and filtering system. China Foundry, 2020, 17(2): 178–182.
[3] Yan Q D, Gong X D, Gong W B, et al. Lightweight innovation ADIs help development of renewable energy and new technology industries in China. China Foundry, 2024, 21(5): 507–515.
[4] Katuku K. Regime features of austempered ductile iron cutting. Journal of Manufacturing Processes, 2022, 83: 374–386.
[5] Vicente A D, Moreno J R S, Santos T F D, et al. Nucleation and growth of graphite particles in ductile cast iron. Journal of Alloys and Compounds, 2019, 775: 1230–1234.
[6] Ghassemali E, Hernando J C, Stefanescu D M, et al. Revisiting the graphite nodule in ductile iron. Scripta Materialia, 2019, 161: 66–69.
[7] Alonso G, Tokarski T, Stefanescu D M, et al. On the crystallography of the Mg-Si-Al nitride nuclei and of the graphite/nitride interface in spheroidal graphite iron. Carbon, 2022, 199: 170–180.
[8] Yao M X, Xue J, Huang H, et al. Study on the effect of ultrasonic treatment for fabricating nodular cast iron with improved mechanical properties. Journal of Materials Research and Technology, 2024, 29: 5295–5303.
[9] Horbach L, Zhang J, Sedlatschek T, et al. The effect of silicon on the critical resolved shear stress of solid solution strengthened ferritic ductile iron. Materials & Design, 2024, 244: 113130.
[10] Wigger T, Andriollo T, Xu C, et al. In situ synchrotron investigation of degenerate graphite nodule evolution in ductile cast iron. Acta Materialia, 2021, 221: 117367.

[11] Yi P Y, Guo E J, Wang L P, et al. Microstructure and mechanical properties of two-step Cu-alloyed ADI treated by different second step austempering temperatures and times. China Foundry, 2019, 16(5): 342–351.
[12] Regordosa A, de La Torre U, Sertucha J, et al. Quantitative analysis of the effect of inoculation and magnesium content on compact graphite irons – Experimental approach. Journal of Materials Research and Technology, 2020, 9(5): 11332–11343.
[13] Alonso G, Stefanescu D M, Bravo B, et al. Effect of tellurium on the nucleation process of spheroidal graphite in cast iron. Journal of Materials Research and Technology, 2022, 19: 4451–4462.
[14] Liu J H, Yan J S, Zhao X B, et al. Precipitation and evolution of nodular graphite during solidification process of ductile iron. China Foundry, 2020, 17(4): 260–271.
[15] Kaymak K, Tazegül Y, Keyvanklı A B, et al. Effects of Ti addition and wall thickness on microstructure, hardness, and wear properties of spheroidal graphite cast irons. Tribology International, 2024, 195: 109612.
[16] Bauer B, Pokopec I M, Petric M, et al. Effect of cooling rate on graphite morphology and mechanical properties in high-silicon ductile iron castings. International Journal of Metalcasting, 2020, 14(3): 809–815.
[17] Górny M, Tyrała E. Effect of cooling rate on microstructure and mechanical properties of thin-walled ductile iron casting. Journal of Materials Engineering and Performance, 2013, 22(1): 300–305.
[18] Anca D E, Stan I, Riposan I, et al. Graphite compactness degree and nodularity of high-Si ductile iron produced via permanent mold versus sand mold casting. Materials, 2022, 15(8): 2712.
[19] ISO, Microstructure of cast Irons – Part 4: Determination of nodularity in spheroidal graphite cast irons. International Standard Organization (ISO), Switzerland, Geneva, 2019.
[20] Caballero F G, Garcia-Mateo C, Santofimia M J, et al. New experimental evidence on the incomplete transformation phenomenon in steel. Acta Materialia, 2009, 57(1): 8–17.
[21] Du Y Z, Gao X Q, Wang X L, et al. Tribological behavior of austempered ductile iron (ADI) obtained at different austempering temperatures. Wear, 2020, 456: 203396.
[22] Bauer B, Mihalic Pokopec I, Mrvar P, et al. Influence of chemical composition and cooling rate on chunky graphite formation in thick-walled ductile iron castings. International Journal of Metalcasting, 2023, 17(3): 2050–2061.
[23] Xu C, Wigger T, Azeem M A, et al. Unraveling compacted graphite evolution during solidification of cast iron using in-situ synchrotron X-ray tomography. Carbon, 2021, 184: 799–810.
[24] Angella G, Ripamonti D, Górny M, et al. The role of microstructure on tensile plastic behavior of ductile iron GJS 400 produced through different cooling rates, Part I: Microstructure. Metals, 2019, 9(12): 1282.
[25] Liu J H, Xiong P, Fu B G, et al. Effects of austempering temperature on microstructure and surface residual stress of carbidic austempered ductile iron (CADI) grinding balls. China Foundry, 2018, 15(6): 173–181.
[26] Wang T T, Yang S F, Li J F, et al. Effect of in situ observation of cooling rates on acicular ferrite nucleation. High Temperature Materials and Processes, 2022, 41(1): 181–190.
[27] Bevilaqua W L, Epp J, Da Silva Rocha A, et al. Explaining the abnormal dilatation behavior during the austenite formation in a microstructure of a low-carbon low-alloy steel containing retained austenite. Metallurgical and Materials Transactions: A, 2003, 54(8): 3349–3357.
[28] Wang X, Du Y, Liu B, et al. Enhanced plasticity of austempered ductile iron (ADI) by partitioning treatment. Materials Science and Engineering: A, 2021, 804: 140513.
[29] Schouwenaars R, Kestens L A I. Dislocation pileups in small grains. International Journal of Plasticity, 2023, 164: 103602.
[30] Li J, Wang Z, Zhang N, et al. Crack-tip plasticity mediated grain refinement and its resisting effect on the fatigue short crack growth. International Journal of Plasticity, 2024, 181: 104102.
[31] Tong L F, Zou Q C, Jie J C, et al. Wear behavior of ductile iron wheel material used for rail-transit vehicles under dry sliding cnditions. Material, 2020, 13(12): 2683.
[32] Dai P Q, He Z R, Zheng C M, et al. In-situ SEM observation on the fracture of austempered ductile iron. Materials Science and Engineering: A, 2001, 319: 531–534.
[33] Liang X M, Xing Y Z, Li L T, et al. An experimental study on the relation between friction force and real contact area. Scientific Reports, 2021, 11(1): 20366.